Lagrangian marker particle trajectory and microconductivity measurements in a mixing tank

D.F. Scofield[a], Pablo Huq[b],*

[a]Department of Physics, Oklahoma State University, Stillwater, OK 74078, USA
[b]College of Marine and Earth Studies, University of Delaware, Newark, DE 19716, USA

A B S T R A C T

Large regions of inhomogeneous mixing have been observed in industrial, bottom-sweeping impeller crystallizers. To investigate this phenomenon, we conducted experiments on a one-tenth volume model of this kind of mixing tank. Results are reported of Lagrangian marker particle (LMP) and microconductivity measurements using the model mixing tank with impeller tip Reynolds numbers of 25,000. Surprising structure is found in this high Reynolds number flow. Using the LMP trajectory data, we show the flow consists of a narrow region of rapidly moving, upward spiralling flow at the tank perimeter. This flow returns slowly through a vertical stack of tori and through a quiescent region centered on the impeller. These tori are concentric with the impeller and exist at loci of regions of shear found adjacent to the quiescent central region and the tank perimeter.

Conditional analysis of the microconductivity signals reveals that large concentration fluctuations occur in the perimeter flow. In contrast, only small diffusive-like concentration fluctuations occur in the center of the tank. This segregation of regions of rapid transport in the perimeter flow from regions of micromixing in the quiescent region results in inhomogeneous mixing in the tank. The complexity of the flow is reflected in the large dynamical dimension (≈ 24) of the flow obtained from the calculation of the Kolmogorov entropy production rate. The return-time distribution was found to be composed of a superposition of two log-normal distributions. Period doubling phenomenon was also found in these distributions.

© 2008 Elsevier Ltd. All rights reserved.

1. Introduction

Stirred tanks are commonly used in industry as chemical reactors and crystallizers. These tanks are often called continuously stirred tank reactors (CSTRs) or stirred tank reactors (STRs). The homogeneity of mixing in these tanks is an important determinant of the quality of products produced in them. Thus, there is a practical motivation to improve our understanding of mixing in these tank flows. The motivation for the present study are observations by industrial plant operators of inhomogeneous mixing in the stirred tanks employed in producing the silver halide (AgCl, AgBr) crystallites used in the manufacture of photographic emulsions. These industrial crystallizers use bottom-sweeping impellers so that the crystallites do not accumulate on the bottom of the tank. The immediate problem is to understand the incomplete mixing and variable precipitation rates found in large volumes of the center of the tank. It was further noticed that there were well-defined regions in the tank where the reactant profiles differed markedly from other regions in the tank. Our earlier studies on a tank with a Rushton impeller located at the tank mid-height (Togatorop et al., 1994) showed no evidence of such incomplete mixing. Thus, the macroscopic flow field of the Rushton and the bottom-sweeping impeller differ significantly. This focused attention on determining the flow field of the bottom-sweeping impeller arrangement. Relatively little is known about the flow field of bottom-sweeping impellers. The experimental results reported here for a 280 l tank with a bottom-sweeping impeller provided ample evidence of inhomogeneous mixing in the center of the tank.

In applying theoretical and experimental methods in mixing fluid flows, one is immediately confronted with a choice of using either Eulerian field based approaches or Lagrangian marker particle (LMP) based methods. This paper describes the combination of experimental and theoretical methods for characterizing turbulent mixing in mixing tanks with bottom-sweeping impellers using flow following LMP and more traditional multipoint Eulerian microconductivity probe techniques.

Our experimental results illustrate the synergy of the LMP and microconductivity approaches in the analysis of mixing. The results

* Corresponding author.
   E-mail address: huq@udel.edu (P. Huq).

reported are for high Reynolds number flow (tip Reynolds number approximately 25,000). We find that the structure of the flow field with a bottom-sweeping impeller consists of an outer, large swirl surrounding a central annulus around the impeller shaft. The inner annular region does not mix well with the outer, main swirl flow. Between the outer, large swirl and the inner annulus are shear flow zones composed of stacks of small tori. The persistence of such structures in high Reynolds number flows is a significant characteristic of the mixing tank with a bottom impeller. Such structures are not usually detected by standard statistical averaging methods because the averaging process itself smooths out the information of coherent structures.

This paper is organized into five parts. Following this Introduction, we provide a brief background of relevant work on mixing in tanks. Section 3 summarizes the theoretical methods that we have found useful in characterizing the flows. The experimental methodology and results are discussed in Section 4. The final section provides a summary and conclusions.

2. Background

The idea of viscous subranges for scalar mixing in isotropic turbulence was introduced in Batchelor (1959). This is applicable to tank mixing problems as an approximation. It has been shown by Bourne and Dell'ava (1987) that significant chemical reactions occur only when micro-mixing takes place (i.e., for length scales in the viscous-convective and viscous-diffusive subranges). It is known that the turbulent flow field is weaker (i.e., anisotropic and inhomogeneous) in certain regions of a tank. The practical problem is that the geometry and boundaries of the vessels containing the flows of interest are complicated leading to a structuring of the turbulent flow in the tank.

Central to understanding turbulent mixing processes (macro- and micro-mixing) is how fluid moves about in a tank as this determines the efficacy of mixing. The large-scale (macro) flow which transports reactants and fluid parcels within the tank is determined by the geometry of the tank and geometry and location of the impeller. Micro-mixing which controls the rates of molecular mixing and reaction depends on the magnitude of kinematic viscosity v and kinetic energy dissipation rate $\mathscr{E}_{TKE}$. Estimation of $\mathscr{E}_{TKE}$ is not easy. From their particle-image velocimetry (PIV) studies with a Rushton impeller (Sharp and Adrian, 2001; Escudié and Liné, 2003) showed the assumption of isotropy can lead to an over estimation of the true dissipation rate. Secondly, reliance on spatially averaged values of dissipation is insufficient as local values of dissipation govern many processes. For a mixing tank powered by a Rushton impeller (Ducci and Yianneskis, 2005) determined using laser Doppler anemometry that local values of $\mathscr{E}_{TKE}$ varied considerably with radial and vertical distance away from the impeller. Similar studies have yet to be undertaken for other configurations such as the bottom-sweeping impeller.

To investigate macro- and micro-mixing for the bottom-sweeping impeller we employ two complementary approaches. The LMP method allows the determination of the large-scale structure, while micro-conductivity probes yields information on small-scale mixing. Conductivity probes are routinely used in mixing tank studies. For example, Reilly and Britter (1985) determined from their conductivity measurements that there is no effect of the Reynolds number on the dimensionless mixing time $N \times t$ where N is the rotation speed of the impeller and t is the measurement time. There are few reported studies with LMP data for high Reynolds number flow.

Numerical (Aref, 1986, 1988) and experimental (Ottino et al., 1988) studies of Lagrangian mixing have been reported for two-dimensional systems at low Reynolds number. The term chaotic advection has been applied to the motion of particles in fluid mixing

(Aref, 1984, 1990). Mixing and the kinematics of chaotic advection, from a modern perspective, is typically based on analysis of multiple, simultaneously present, marker particles. In contrast, at this stage of our work, we prefer to use one particle and invoke the hypothesis of "ergodicity" (Eckman and Ruelle, 1985) to simplify the experiment. This hypothesis is equivalent to the assertion that the information gained from measuring a single particle for a long time in a bounded vessel is the same as that obtained from measuring many particles simultaneously for a short time interval. The *ergodic hypothesis* allows us to use the single particle LMP data to map out the flow (Dombre et al., 1986). The trajectory of the LMP yields a chaotic position and velocity signal. We utilize tools from the emerging science of nonlinear dynamical analysis to understand this position and velocity signal. A useful review of the analysis of chaotic signal data is by Abarbanel et al. (1993) and Abarbanel (1996). Analysis of signals in terms of the dimension of the underlying flow manifold was studied by Broomhead and King (1986) and Broomhead and Jones (1989). The approaches in Wittmer (1996), Gilmore (1998), Letellier et al. (1995) and Letellier and Aguirre (2002) are close in spirit to ours.

3. Theoretical methods

In this section we outline the theoretical methods employed to understand mixing in a tank with a bottom-sweeping impeller. Results from applying these methods are given in the following section. The detailed statistical results we are able to obtain provide new perspectives from which to view the structure of high Reynolds number turbulent fluid flows in CSTRs. The statistical measures we describe include Kolmogorov entropy production rate calculations, mixing time distribution, return-time distribution, and probability measures. The basis of many of our calculations relies on the embedding of the LMP flow data into higher than three-dimensional spaces. The embedding allows determination of the complexity or dimensionality of the flow. Thus, we first describe this embedding process, then the statistical methods used.

3.1. Embedding the experimental data

The dimension of the embedding space is a measure of the complexity of the flow. It can be shown that the problem of obtaining the structure of the flow involves a multi-dimensional space and this space can be obtained by embedding the sampled-path data using the Whitney embedding theorem. The practical implementation of the Whitney embedding can be approached using the Takens–Mañé theorem (Mañé, 1981; Takens, 1980).

The Takens–Mañé theorem shows, given a LMP trajectory, $x(t)$, time (t)-sampled data with sampling interval τ, that one can form the sequence of m_{bed}-dimensional position vectors

$$x_1 = (x(t), x(t-\tau), \ldots, x(t-(m_{bed}-1)\tau))$$
$$x_2 = (x(t-\tau), x(t-2\tau), \ldots, x(t-(m_{bed}-0)\tau))$$
$$\vdots \quad = \vdots \quad \vdots \tag{1}$$

and this forms a $3m_{bed}$ dimensional Whitney embedding of the original sampled data set. The dimension m_{bed} is called the number of degrees of freedom. It gives the number of three-dimensional nonlinear dynamical equations required to locally describe the dynamical system. We have gone from a three-dimensional space to one where each point x_i has $3m_{bed}$ components. This is called the method of delays. The delay intervals are $0\tau, 1\tau, \ldots, (m_{bed}-1)\tau$. Thus, once the embedding dimension m_{bed} is chosen large enough and an appropriate delay interval found, the physical properties of the equivalent dynamical system generating the path can be extracted using the time delay coordinates. The embedding dimension is also calculable

using statistical methods involving the Kolmogorov entropy as we describe next.

3.2. Kolmogorov entropy

The Kolmogorov entropy production rate $\dot{K}$ provides a measure of the mixing in the tank. It provides a measure of the temporal disorder, i.e., dynamical randomness, in both deterministic dynamical systems and stochastic processes (Andrieux and Gaspard, 2007). The Kolmogorov entropy production rate itself has the following properties:

$\dot{K} = $ zero: an ordered system (laminar),

$\dot{K} = $ finite: transitional (chaotic),

$\dot{K} = $ infinite: totally random (truly turbulent). $\qquad(2)$

We note that a quantity, $\dot{K}_2$, provides a lower bound to the Kolmogorov entropy production rate (Grassberger and Proccacia, 1983):

$$0 \leqslant \dot{K}_2 \leqslant \dot{K} \qquad (3)$$

and satisfies the same conditions as $\dot{K}$. The quantity $\dot{K}_2$ has been shown to be calculable (as $\varepsilon \to 0$) as follows (Grassberger and Proccacia, 1983). First define the *correlation integral* $C_n(\varepsilon)$ as the limit as $N \to \infty$ of the ratio

$$C_n(N, \varepsilon) = \frac{\text{total number of pairs at or within radius } \varepsilon}{\text{largest number of mathematically possible pairs}}$$
$$= \frac{(\text{number of pairs } (i,j) \text{ with } \|\mathbf{X}_{in} - \mathbf{X}_{jn}\|_{3n} < \varepsilon)}{N(N-1)/2}. \qquad (4)$$

That is

$$C_n(\varepsilon) = \lim_{N \to \infty} C_n(N, \varepsilon). \qquad (5)$$

Then define

$$\dot{K}_{2,n}(\varepsilon) = \frac{1}{\tau} \ln \frac{C_n(\varepsilon)}{C_{n+1}(\varepsilon)}. \qquad (6)$$

Here $C_n(\varepsilon)$ has been shown to behave as (Grassberger and Proccacia, 1983)

$$C_n(\varepsilon) \approx \lim_{\varepsilon \to 0} \varepsilon^n \exp(-n\tau \dot{K}_2). \qquad (7)$$

Here the distance or norm between the pairs of points $\mathbf{X}_i$ and $\mathbf{X}_j$ in a $3n$-dimensional space is denoted by the real quantity $\|\mathbf{X}_{in} - \mathbf{X}_{jn}\|_{3n}$. This norm is the distance between two delay path vectors $\mathbf{X}_i = (\mathbf{X}_i, \mathbf{X}_{i+1}, \dots, \mathbf{X}_{i+n-1})$ and $\mathbf{X}_j = (\mathbf{X}_j, \dots, \mathbf{X}_{j+n-1})$. The number $3n$ is thus an embedding dimension and n is the number of degrees of freedom. Here N is the number of three-dimensional vectors in the record considered from the experimental data set. The quantity $3n$ serves as an estimate of the embedding dimension. This has become the standard practice in the analysis of observed chaotic data (Abarbanel et al., 1993; Abarbanel, 1996).

The Kolmogorov entropy production rate measures the average dispersal of particles from any elementary volume in a closed region of flow. It gives the temporal average rate of entropy production or information loss at a point. It complements the insight gained from the return-time distribution described below. The results can be displayed to indicate the positions in a tank where the entropy production is least, etc. The quantity $\dot{K}_2$, in the limit of large time $t_n = n\tau$, can thus be interpreted as a "mixing time constant".

3.3. Mixing time

A practical definition of good mixing is that solutions added at a point in a tank be rapidly and thoroughly dispersed throughout. Thus, there are two aspects of the problem: thoroughness of dispersal and rapidity. There is a third aspect, namely, that in a tank these properties can depend on position—these properties are Eulerian field quantities. The thoroughness aspect can be addressed by using concepts related to production of disorder.

Turbulent dispersal can be viewed as a stochastic process. However, it is not random and it is recognized that coherent structures play a significant role in the dispersal of particles. Our experimental results show that coherent structures in the form of tori indeed do affect the dispersal process. One can develop a pragmatic analysis of the thoroughness of dispersal property along the following lines. Place a number Q of particles into an initial volume V_0 of a stirred tank. Following the group of particles, one would find after a time interval Δt that the particles would occupy a (larger) volume V_1. The probability that one particle would be observed in a volume corresponding to the original volume V_0 would be (V_0/V_1). The (small) probability that all Q particles would be observed in V_0 is then $(V_0/V_1)^Q$. This leads to the definition of a mixing entropy change ΔS as can be seen in the following. As the particles' average distance increases, there is a change in the volume in going from the initial volume V_0 to the expanded volume V_1. This leads to a change in entropy that is proportional to the logarithm of the fractional volume change

$$\Delta S = S_{final} - S_{initial} = Qk_B \ln\left(\frac{V_1}{V_0}\right) = -Qk_B \ln\left(\frac{V_0}{V_1}\right), \qquad (8)$$

where k_B is Boltzmann's constant and Q is the number of particles in the volume as stated above. This is a measure of thoroughness: best mixing occurs when ΔS is maximized. Clearly if a set of added particles is merely convected by the flow, no mixing has occurred, the flow has merely stirred the particles by moving them from one point to another and $V/V_0 = 1$, so $\Delta S = 0$.

In mixing, one is not just interested in the final increase in entropy as just discussed but is also interested in the rate or rapidity of entropy production. Thus, one wants to know how fast ΔS increases from its initial zero value to its maximum value. That is, one needs a measure of the time rate of change of the dispersal of a group of particles in the tank. This more detailed computation is related to the correlation integral, $C_n(\varepsilon)$, given in Eq. (4) above. The quantity $C_n(\varepsilon)$ can be directly computed as it is related to the number of particles in an n-dimensional space that are closer than a small distance ε. Clearly, the results depend upon N and ε. To avoid this dependence one would like to take the limit as $N \to \infty$ and $\varepsilon \to 0$. That is, one would like the dispersal entropy in terms of a continuous distribution of added particles and the resolution ε to be as tight as possible. The time rate of change of $\ln C_n(N, \varepsilon)$, i.e., $K_n = (\ln C_n(N, \varepsilon) - \ln C_{n+1}(N, \varepsilon))/\tau$, where τ is the sampling rate (averaged over the fluctuations), gives an entropy production rate. The time constant of entropy production is a measure of the mixing time. This (Kolmogorov) entropy production rate depends on the location in the tank, so it is a field quantity.

3.4. Return-time distribution

There is yet another aspect of mixing that is important. It is the time required for a particle leaving a high reactant concentration region to return to it. This is important because here the reaction rates depend on position in a tank. A crystallizer accentuates this because there are large concentration gradients maintained in a tank due to the high concentration of reactants provided at the feed jets.

In general, the time it takes for particles initially in a source region to find their way to a destination region defines a transit time. When the source and destination are in the same region, there is defined a return-time. The distribution of these return-times can be displayed in a histogram called a return-time (frequency) distribution. The abscissa axis of the plot of the distribution of return-times is proportional to the logarithm of the return-time—a consequence of fluctuating, globally bounded, locally exponential divergent LMP paths (Aitchison, 1966). Given sufficient LMP data, a return-time distribution can be computed.

3.5. Frequency and probability measures

Because of the extensive LMP path data set available for analysis, other measures can be computed. For example, the frequency distribution of finding the LMP in a small volume and joint probability of two particles meeting at a location can be computed. Such calculations can be extended to the joint probability distributions of three or more particles as well. We can also compute Poincaré sections of the turbulent flow. These results can be used in the placement of feed jets and the design of automatic control strategies to optimize yields.

4. Experiment

4.1. Experimental setup

Experiments were performed on the single bottom-sweeping impeller driven flow in a cylindrical tank diagrammed in Fig. 1. That figure depicts a tank of height 102 and 60 cm in diameter (approximately 280 l in volume). Located at the bottom of the tank, sweeping the bottom, is a four sided, flat blade impeller. The impeller is powered by a constant power pneumatic motor to generate a flow with constant energy dissipation. The bottom-sweeping impeller rotates at 50 rpm. Reynolds numbers at the blade tip exceeds 25,000, so the flow is fully turbulent. The tank is surrounded by a rectangular outer tank whose purpose is to provide distortion free optics for particle following. This is implemented by filling the gap between the tank and the outer tank with fresh water at the same temperature as the inner tank.

The choice of the diameter of the LMP is dictated by the need to track a marker particle over a viewing window about 1 by 1 m in size. This meant that we could not use particles of order 10 μm diameter that are typically used for LDA and PIV measurements. After experimenting with many other diameters we settled on a LMP of diameter 0.4 cm to facilitate practical simultaneous tracking of the LMP on the three video cameras that were used to record the experiment. The LMP consisted of a 0.4 cm diameter neutrally buoyant mixture of carbon black and bee's wax. The value of the Stokes number ($St = 2a^2 U/9\nu L$) is less than one. Here a is the LMP radius, L is a characteristic length scale, taken to be the radius of the tank, U, a characteristic velocity of 30/cm s^{-1}, and ν the kinematic viscosity of water, 0.01 cm^2/s. Corrections to the trajectory of LMP due to inertia of the neutrally buoyant particle been shown to be negligible in this range of Stokes number (Maxey and Riley, 1983; Maxey, 1988; McLaughlin, 1988). Corroborating this is the fact that dye streaks in the vicinity of an LMP showed no measurable differences from the trajectory of the LMP itself.

Three orthogonally arranged (NSTC) video cameras were used to synchronously track the LMP from the x,- y- and z-planes. The three views permit tracking the LMP from at least two cameras at all times, even in the presence of the opaque impeller shaft. LMP position time series data were collected for up to 100 h. This duration is sufficient to provide binning with more than 50 samples in each bin. This allows resolution of period doubling in the

distribution of return-times. A computer and frame grabber allowed direct calculation of the position of the particle in a two-dimensional view. The spatial resolution of the cameras is sufficient to resolve 0.1 cm × 0.1 cm square pixels in the viewing plane. This is more than sufficient to resolve the LMP. Frames were collected at a 66 Hz rate and the trajectories were cubic spline fit through five data points to accurately place the particle position. The LMP particle paths are corrected for parallax and Snell's Law.

The microconductivity probes were placed at a distance of 30 cm from the bottom, and at 10 and 20 cm from the wall of the cylindrical tank, i.e., 10 and 20 cm, respectively, from the axis of the impeller shaft. The experiments with the microconductivity apparatus involve introducing a liter of brine, of density 1100 kg/l, at a location on the perimeter of the cylindrical tank opposite the conductivity probes. Each experimental run was conducted three times to verify repeatability. The spatial resolution of the conductivity probe is of order 0.01 cm and the temporal resolution is 100 Hz. This is sufficient to resolve the spectrum of scalar fluctuations to the Kolmogorov scale.

4.2. Experimental results

The schematic of the flow driven by the bottom-sweeping impeller is shown in Fig. 1b. The flow consists of an outer or perimeter swirl enveloping a stack of nested tori. This outer swirl constitutes the *main toroidal flow*. This rapidly swirling flow spirals upward in a narrow region along the vertical walls of the tank. Its downward return covers a larger horizontal cross-sectional area and moves more slowly. Between the outer spiral flow and the center of the tank are vertically stacked tori or coherent structures which are circular in plan and concentric with the impeller. The main toroidal flow envelopes a (secondary) set of two concentric, nested stacks of tori. A schematic emphasizing the relative sizes of the main toroidal flow and the stacked, nested toroidal flow is given in Fig. 1c. Even with a high Reynolds number, it is seen that there is considerable structure to the flow.

The evolution of trajectories of particles emanating from a small volume can be simulated by collecting LMP paths that flow through a small volume. Such a simulation is shown in Fig. 2. The sequence of figures (from the top left to the bottom right) shows the growth of the paths of the particles in time. In these figures a general swirling flow in a clockwise direction viewed from the top is evident.

Fig. 3a shows the LMP paths seen from the top and Fig. 3b shows the path seen from the side. This top view shows the projection of both upward moving part of the LMP trajectory and downward moving parts of the trajectory. There is an absence of paths in the center of the tank. The side view, Fig. 3b, shows that the impeller pumps fluid from the bottom of the tank forcing the fluid to spiral upwards in a narrow region along the walls toward the top.

Fig. 4 shows the radial distribution of the Eulerian velocity components at a location approximately halfway up the tank ($z \approx 0$) from the bottom. The figure gives averaged values of v_z, v_θ, and v_r. Notice first that none of the velocity components deviate measurably from zero in the central region for radii in the range $0 \leqslant r \leqslant 7.6$ cm; this is called the "dead zone" because of this small velocity field. For all velocity components there is a region of large variability in the range $7.6 \leqslant r \leqslant 11.4$ cm: this is a region of shear flow. Values of vertical velocity v_z are negative (i.e., downwelling flow) between $12 \leqslant r \leqslant 20.5$ cm. For $r > 21$ cm toward the outer wall of the tank, values of v_z are positive and large due to centrifugally driven upwelling: thus the width of the region of centrifugally driven upwelling is approximately 9 cm. The magnitudes of radial velocity v_r are small everywhere, except in the shear zones in the range $7.6 \leqslant r \leqslant 11.4$ cm and $19.5 \leqslant r \leqslant 22$ cm.

The presence of positive and negative values of v_r is consistent with the presence of toroidal flow with the tori concentric with the
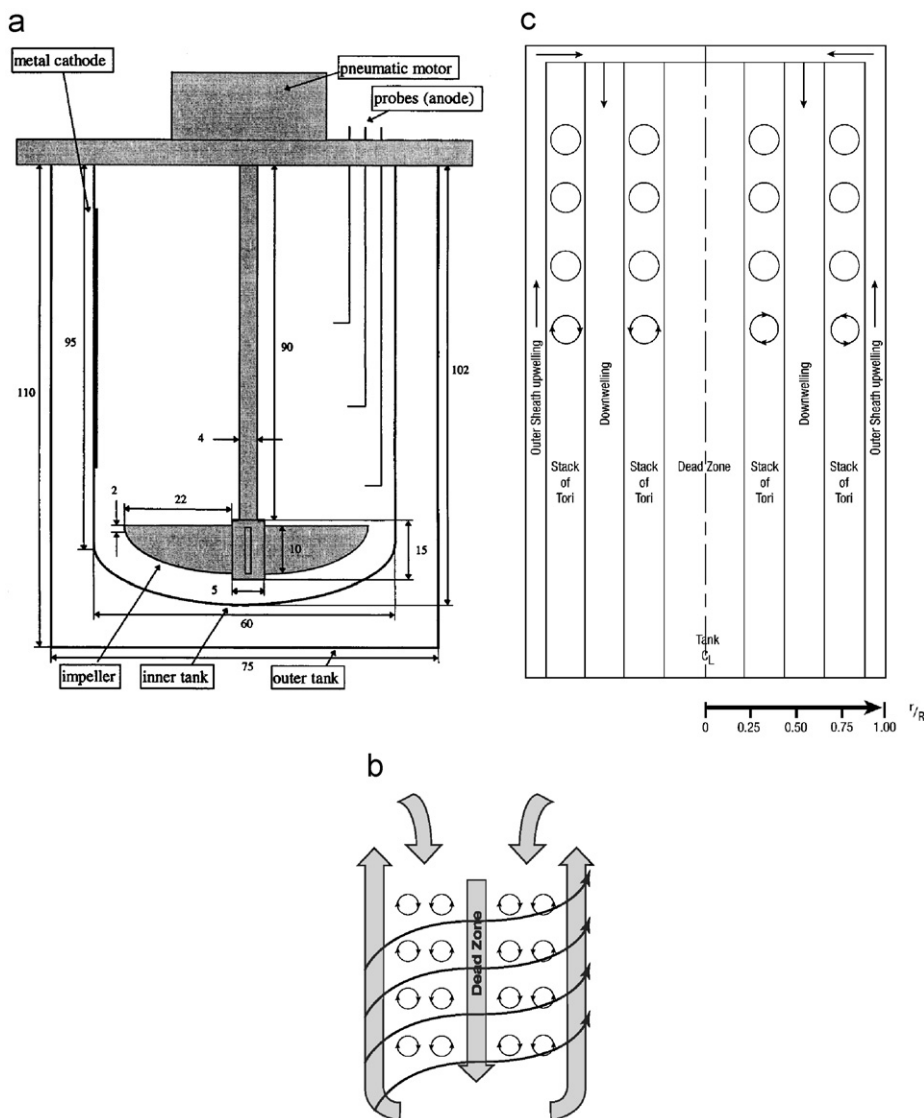
Fig. 1. Schematic of CSTR tank. (a) The tank dimensions holding 280 l. A flat blade (90°, bottom-sweeping) impeller rotating at 50 rpm is used to generate the flow. (b) Overall schematic emphasizing the structure of the flow in the tank. Shown along the tank perimeter is a thin rapidly moving upward swirl region of fluid. At the center of the tank, surrounding the impeller, is a slowly moving downward swirl which we call the dead zone. Between these two regions is a stack of toroidal flow structures. (c) Detailed schematic of the tank flow with a non-dimensional scale r/R. Here R is the radius of the tank. Shown are the outer upwelling sheath at the tank perimeter. At the center is a slowly descending flow that we call the dead zone. Between these two flow regions are two vertical stacks of tori concentric with the impeller shaft.

impeller shaft. The largest values of tangential velocities v_θ occur near the shear zones and decrease to small values elsewhere. The velocity field in the shear zone does not have averages that are stationary. This is the result of intermittency of the flow field involving the secondary tori. This aperiodic flow represents a zone of unstable flow between the so-called dead zone of the tank and the upwelling zone defined by positive z-velocities at the tank perimeter. Note that such non-stationary flows require embedding of the flow into higher dimensional manifolds in order to account for the higher order dynamics observed.

4.3. Kolmogorov entropy and mixing time

A standard metric for evaluating the strength of turbulence is the "turbulent intensity". For instance, we can evaluate this for the tank by using the ratio $v'/\bar{v}_\theta$ of the rms velocity fluctuation, v', divided by the mean radial velocity, $\bar{v}_\theta$. As discussed previously, the aperiodicity

of the flow in the region of shear (see Fig. 4) makes it difficult to estimate stationary values for these quantities. An alternative metric to the "turbulent intensity" is related to the Kolmogorov entropy production rate.

The Kolmogorov entropy production rate is a field quantity that can be computed throughout the tank to determine regions of good and poor mixing. However, these computations are very computationally intensive. One can more easily compute a closely related metric which allows an independent estimate of the (embedding) dimension of the turbulent flow. This is called the correlation integral, $C_n(\varepsilon)$, and it is related to a quantity, $\dot{K}_2$, which provides a lower bound to the Kolmogorov entropy production rate, i.e., $0 \leqslant \dot{K}_2 \leqslant \dot{K}$ (Grassberger and Proccacia, 1983). The fundamental idea is that the flow advances in time in a way that "remembers" its past. Thus the flow at any instant is correlated in a sense with its past. This correlation is computed as a correlation integral of the path with itself delayed for different intervals. As the length of a LMP path increases, the correlation integral limit is given by (Grassberger and
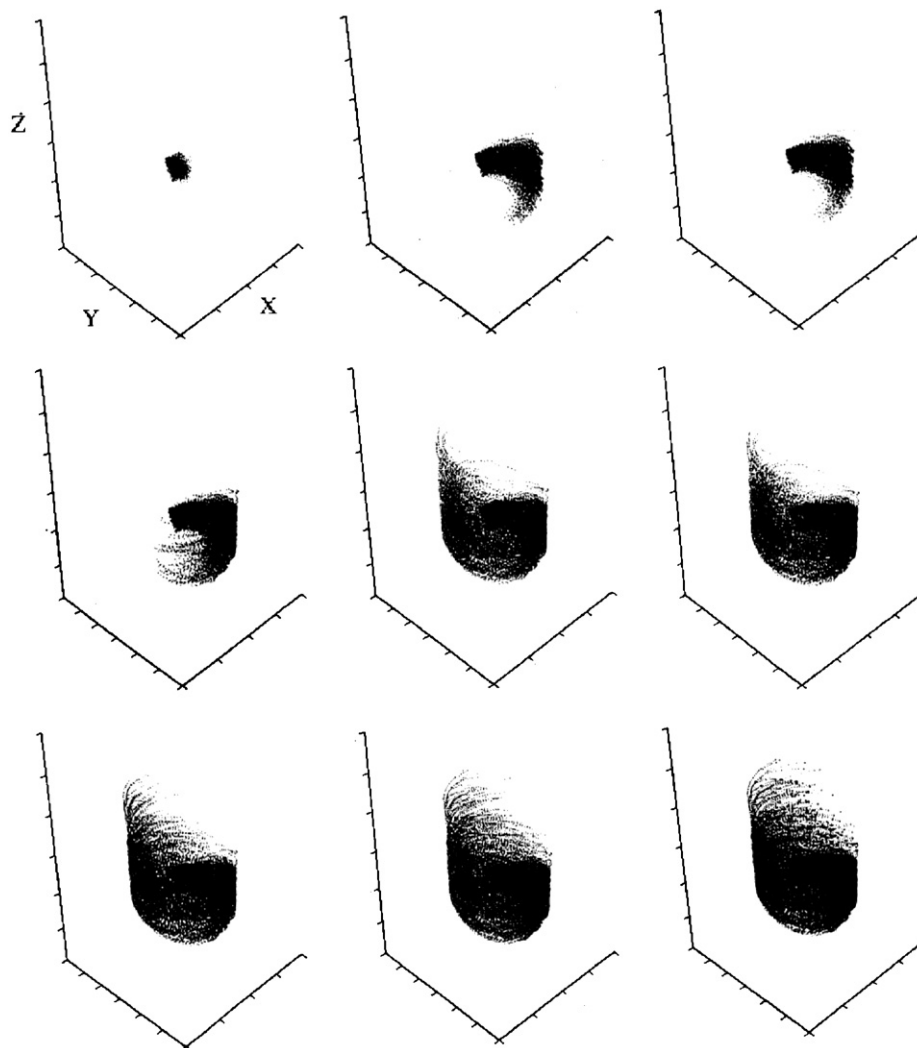
Fig. 2. Dispersion of particle paths in CSTR issuing from a small volume (dye streak simulation). This plot is obtained by collecting paths threading through a small volume, then displaying all of them for increasing time intervals.

Proccacia, 1983)

$$\lim_{N \to \infty} C_n(N, \varepsilon) = C_n(\varepsilon) \approx \varepsilon^n \exp(-n\tau \dot{K}_2), \tag{9}$$

where n is called the correlation exponent. The small quantity ε is a measure of the elemental discretization of the volume. The relation of the limit to the exponential form shows that the correlation rate $\ln C_n(\varepsilon)$ is logarithmically related to $\ln \varepsilon^n = n \ln \varepsilon$. The quantity $3n$ also serves as an estimate of the Whitney embedding dimension.

The Kolmogorov entropy production rate can be computed as an Eulerian field quantity. This can be done by dividing the tank into tetrahedral elements and computing Eq. (4) by choosing a particular cell. This requires restricting the summation over i and j in Eq. (4) to paths emanating from that particular cell, the $\dot{K}_2$ computed is the mixing time constant from that cell. The 280 l tank is tessellated into about 6×10^5 tetrahedra. The Kolmogorov entropy production rate is then computed by finding the particle fluxes through the various tetrahedra then computing the information loss as particles from an elementary volume are dispersed. The correlation integral $C_n(\varepsilon)$ is then computed for increasing time intervals $t_n = nt$. A mixing constant $t_M^{-1} = \dot{K}_2$ can then be obtained (e.g., defined as the limit $N \to \infty$ of $\dot{K}_2$).

The value of the Kolmogorov entropy in terms of $C_n(\varepsilon)$ is finite as shown in the results of Fig. 5. Examination of Fig. 5 shows that the $\log_2 C_n(\varepsilon)$ vs. $\log_2 \varepsilon$ curves get closer and closer together as n increases, piling up in the limit at a value of n slightly above the range $n = 24$–30. This number is related to the embedding dimension described above. The large number reflects the complexity of the flow. In contrast, the Kolmogorov entropy production rate in terms of $C_n(\varepsilon)$ inside the dead zone using LMP data was too small to be computed by the path and box-counting algorithm employed, because of the lack of paths in that region.

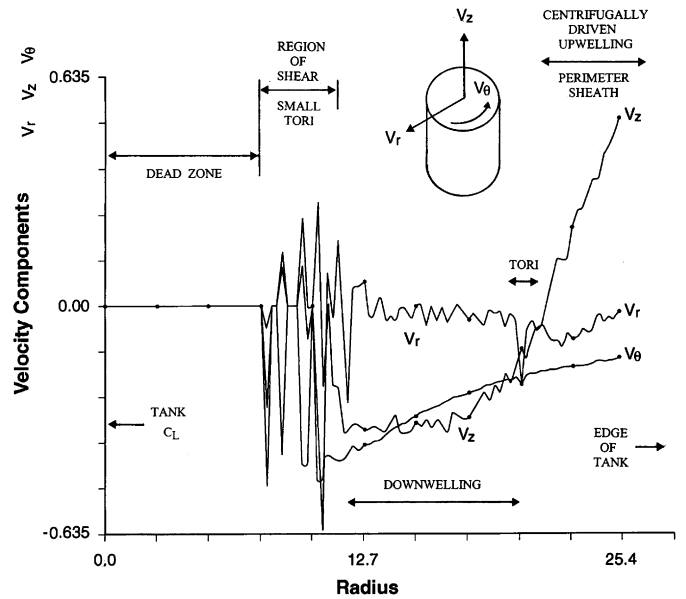### 4.4. Return-time distributions

Return-time distributions have been used in the chemical industry as a measure of mixing. That is, the measurement of the time interval for return of the LMP to a given region provides a metric for the strength of circulation in the tank. The longer the time interval, the weaker the circulation. Fig. 6 shows a return-time distributions measured at a horizontal planar Poincaré-section situated 20 cm above the impeller. The distribution is obtained by histogramming the measured return-times. The vertical axis is the normalized number of times the LMP returns in a certain log-time interval

a

b
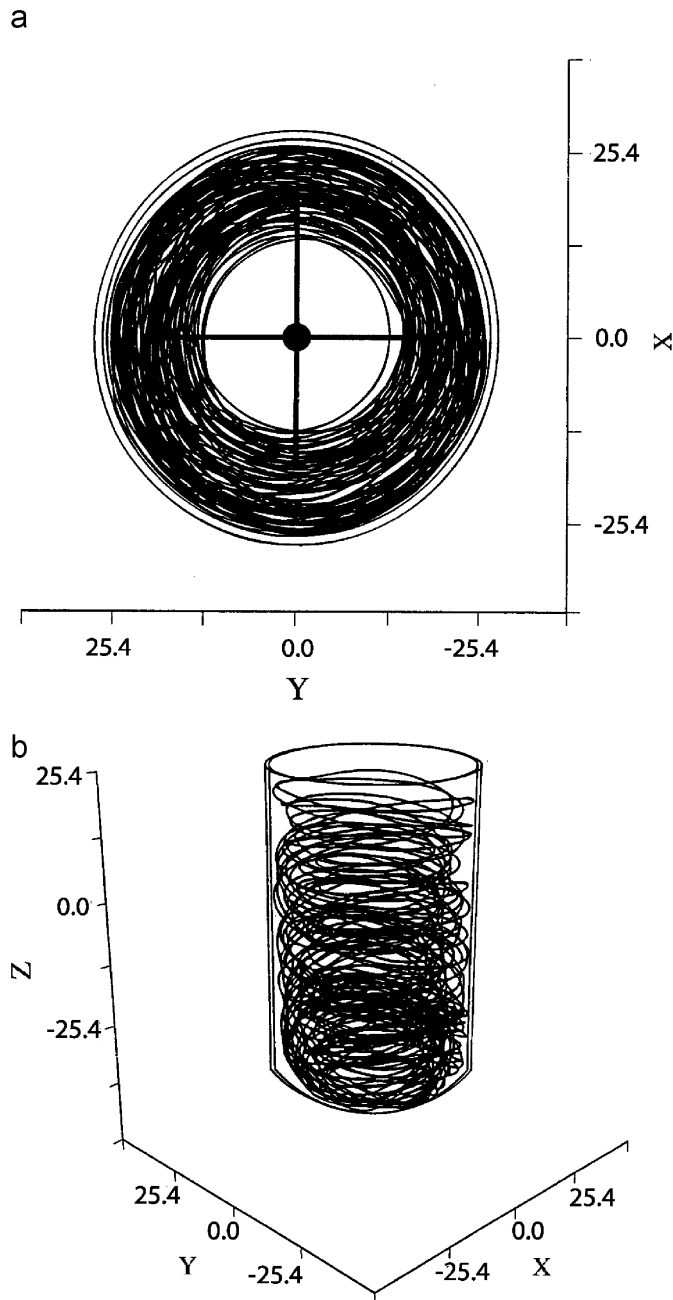
Fig. 3. LMP trajectories in the CSTR. (a) Top view. (b) Side perspective. The top view shows race-track like trajectory for both up-welling and down-welling flow. There is an absence of trajectories in the vicinity of the impeller comprising the dead zone. The side perspective shows the main swirl.

Fig. 4. Computed average Eulerian velocities at mid-height of tank ($z=0$). Along the vertical axes are the radial velocity v_r, the vertical velocity, v_z, and the azimuthal velocity, v_θ, in units of meter per second (m/s). Along the horizontal axis is the radius in units of cm. Near the center of the tank, persistent non-stationary fluctuations in the velocities occur.
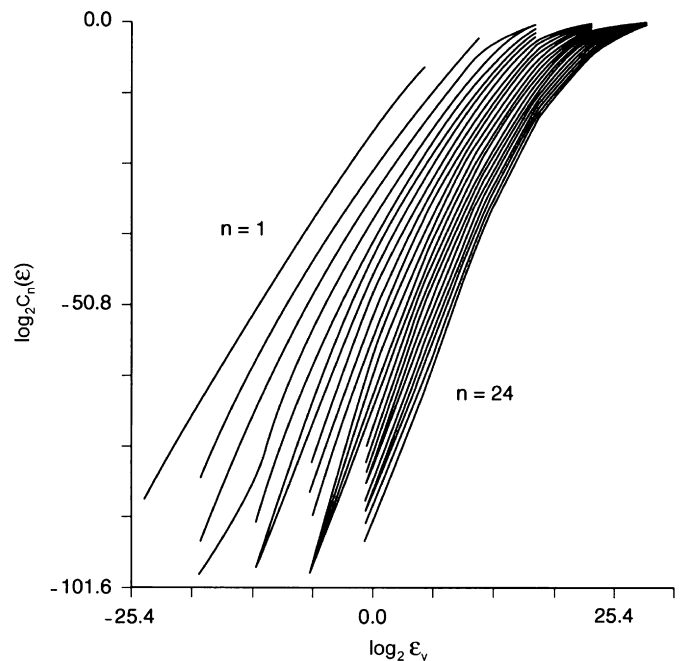
Fig. 5. Change of the lower bound, $\dot{K}_2$, of the Kolmogorov entropy production rate with dimension n. The vertical axis is for the Kolmogorov entropy production rate $\dot{K}_2 \approx \log_2 C_n$. Here C_n is the correlation integral. The horizontal axis is $\log_2 \varepsilon_V$ a logarithmic measure of the box size used in defining the path discretization. The computation uses paths measured at a location 25 cm above the impeller and at a radius of 25 cm from the impeller shaft. This is in the upward swirl region near the perimeter of the tank. The embedding dimension n as shown can be estimated by the pile-up of the traces on the right-hand side of the plot starting around $n \approx 24$.

labeled along the horizontal axis. A superposition of two log-normal distributions are evident in Fig. 6. The left-hand distribution comprises short return-times between 0 and 10 s. whereas the right-hand distribution has a longer return-times up to 80 s. The left-hand log-normal distribution can be ascribed to return paths that quickly return to the Poincaré-section after moving through the impeller region, short-circuiting a path up along the perimeter wall and then back down through the stack of tori (Fig. 1c). When the trajectory is through a stack of tori, the LMP moves relatively slowly: such trajectories yield longer return times found in the right-hand distribution.

The nonlinear interaction of the impeller and the flow is important and gives rise to sub-multiples of the impeller frequency seen
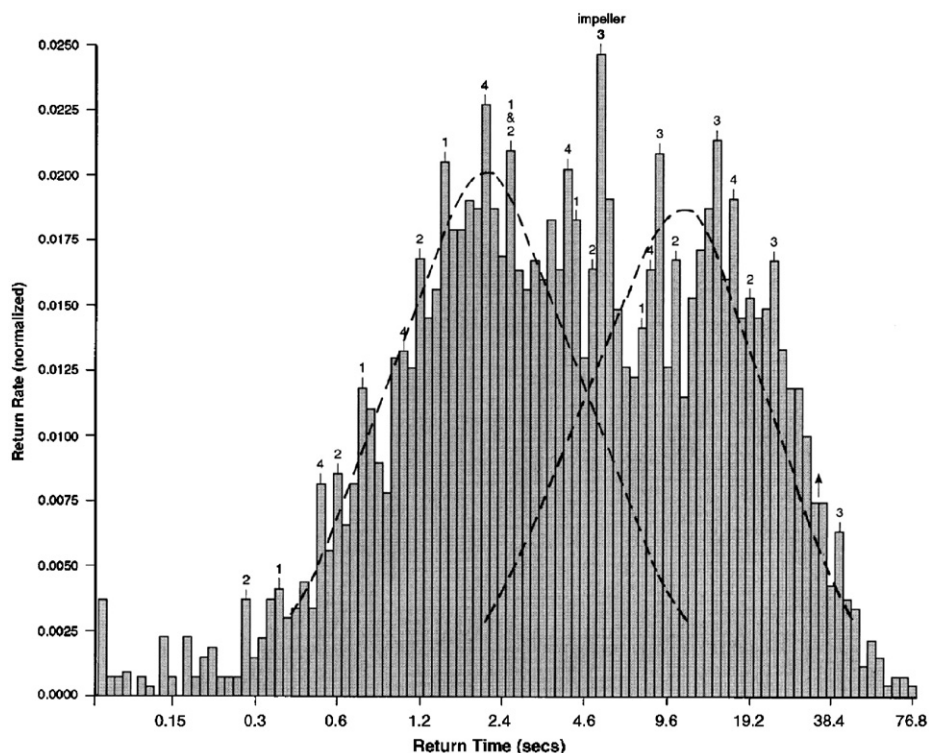
in the return-time distribution. Period doubling or frequency subharmonics are identified as minor peaks (1, 2, 3, 4) in Fig. 6. The peaks have an amplitude that is of the order of 15% greater than background distribution. This is large enough to clearly distinguish them from that distribution. These minor peaks are separated by a

Fig. 6. Return-time distribution (normalized) measured at a horizontal section 20 cm above the Impeller. This return-time is defined as the time interval from exiting a horizontal plane just above the impeller to its return to that plane (Poincaré section). Notice that the sum of the two different (dashed) distributions provide a good fit to the whole histogrammed data.

constant displacement along the logarithmic, horizontal axis. When such a constant displacement occurs along a logarithmic axis, τ, it indicates a multiplicative factor (g) relationship between successive values of τ of the form $\tau_{n+1} = g\tau_n = g^n\tau_0$. The factor $g = 2$ indicates period τ doubling.

Fig. 7 graphs displays a *period doubling relationship* $\tau_{n+1} = 2\tau_n = 2^n\tau_0$ as a straight line for data from the first (1) series. The straight line in Fig. 7 acts as a reflection line having a multiplication factor of (about) two for finding the $(n+1)$th iterate from the nth. The three other series (2, 3, 4) follow the same pattern and are not shown for brevity. The data for the all four cases shows that the minor peaks 1–4 satisfy the same period doubling relation to a high level of accuracy. The intercept at the origin, $\tau_0 = 0.30$ s, is determined from the data as the first iteration factor. This is the period of the successive passes of one of the four impeller blades past a point on the bottom of the tank. The interval corresponding to the impeller rotation rate is labeled "impeller" and lies approximately in the center of the log time axis of Fig. 6. Because of the presence of these period doubling sequences, a picture emerges of flow in which the circulation of the outer swirling (toroidal) flow adjacent to the walls of the tank is synchronized with the impeller motion *and* the rotation of the vertical stack of tori. Period doubling is often found in chaotic systems depending on variation of a system parameter (Eckman and Ruelle, 1985) such as a Reynolds number in a model of fluid flow. In the present case the period doubling occurs without external variation of such a parameter.

### 4.5. Frequency and probability measures

Phase plane plots are useful in exploring interrelationships between a variable and its derivative. By choosing a cylindrical coordinate system centered at the middle of the flow, a surprisingly
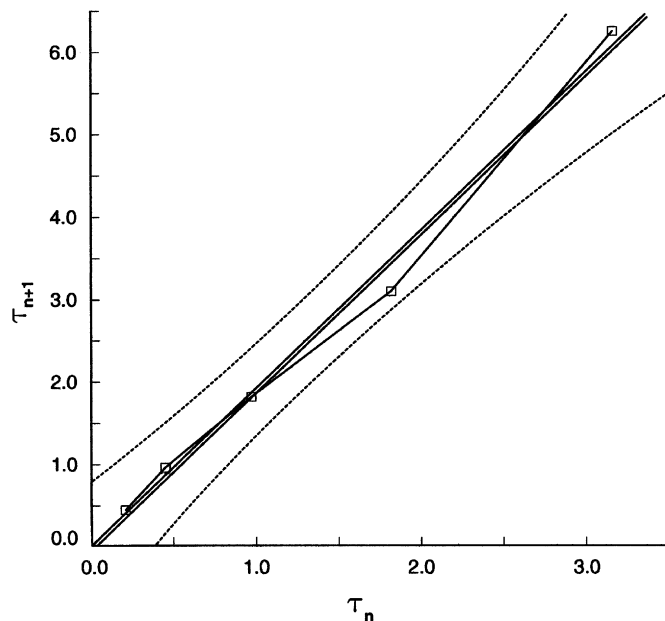
Fig. 7. Return-time, period doubling relationships. Shown are data for the first of four such sequences. The double line is the least squares fit of the experimental data satisfying $\tau_{n+1} = 1.966583\tau_n - 0.041255$. The plot shows the relation between successive return-times in the sequence $\tau^{n+1}/\tau^n \approx 2$. The outer dotted lines give a two standard deviation envelope. The squares are from the experimental data.

simple description of the flow and is obtained by plotting the Poincaré section for the return to a vertical plane through the impeller shaft. Here we first present results for frequency distributions
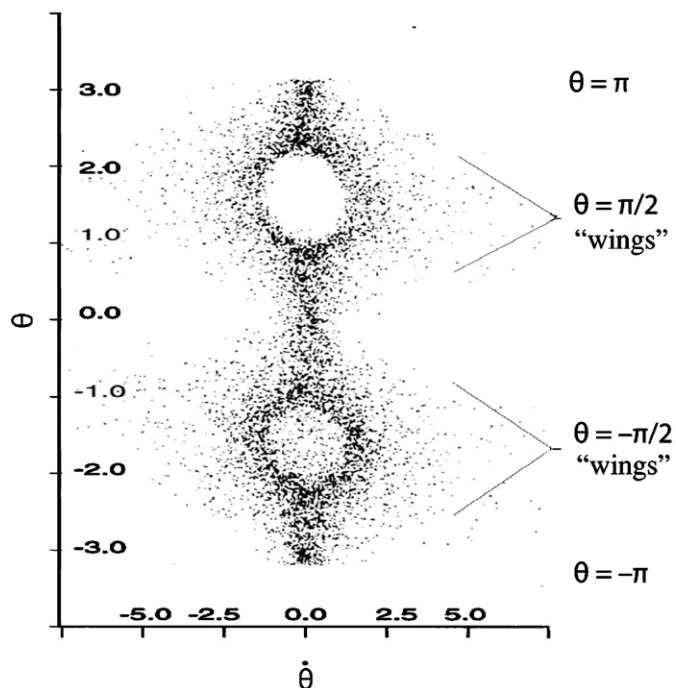
Fig. 8. Experimentally determined toroidal flow structure from Poincaré phase plot. (a) The azimuthal angle $\theta \in (-\pi, \pi)$ vs. its rate of change $\dot\theta$ is plotted. Here the angle variables are the azimuthal angles from the center point of a vertical Poincaré plane aligned through the impeller shaft. The plot of this experimental data shows a cross-section of a torus embedded in a vertical disk. The cluster of dots outside the elliptical holes form a wing-like pattern that are the result of higher dimensional structure in the flow. In the region of the impeller ($\theta = -\pi/2$) there are dots within the torus caused by impeller created turbulence.

Fig. 9. Frequency of finding the LMP at a point in the tank. (a) Vertical position. Data measured at a vertical cross-section centered through the impeller shaft. (b) Dog-bowl shaped distribution for a horizontal x–y plane at a height 20 cm above impeller.

of the LMP passing through planes defined first in the space of the azimuthal angle, $\theta \in (-\pi, \pi)$, along the vertical axis and its rate of change, $\dot\theta$. In the resulting plots, the density of data points plotted provides statistical information as to the frequency of pairs of values $(\theta, \dot\theta)$.

In Fig. 8 we plot the values of the azimuthal angle $\theta \in (-\pi, \pi)$ along the vertical axis vs. against its rate of change, $\dot\theta$, along the horizontal axis. In this figure the angle $\theta = -\pi$, occurs at the bottom of the tank. The top of the flow is represented at the angle of $\theta = \pi$: note there is more dispersion of the dots into the center of the toroid cross-section at $\theta = -\pi/2$. This is the region of the impeller. Furthermore, there can be discerned a distribution of dots above and below the toroidal cross-section centered at $\theta = \pm\pi/2$. These indicate deviations from the main toroidal flow. Examining Fig. 8 more carefully, it is noticed there are small "wings" consisting of scattered dots about $\theta = \pm\pi/2$ in the plotted data. These wings are created by the secondary flow consisting of the stack of tori within the larger, perimeter toroidal flow described above.

These experimental results can be compared to those for typical dynamical systems describing motion of a point on a two-dimensional or higher dimensional mathematical torus. A flow on a two-dimensional toroidal surface can be periodic or quasi-periodic. For a periodic flow, the phase plane portrait is a pattern of separate dots arranged on two circles. The simple mathematical toroidal flow, plotted similarly, would only give two circles centered at $\theta = \pm\pi/2$ if plotted in the format of Fig. 8. In the two-dimensional quasi-periodic case, these dots merge, filling out the circular form. The next step in complexity beyond two-dimensional quasi-periodic flow requires adding a third dimension. Such a flow would be described dynamically as flow on a solid three-dimensional torus. Higher dimensional toroidal flow leads to additional dots and wing-like structures as
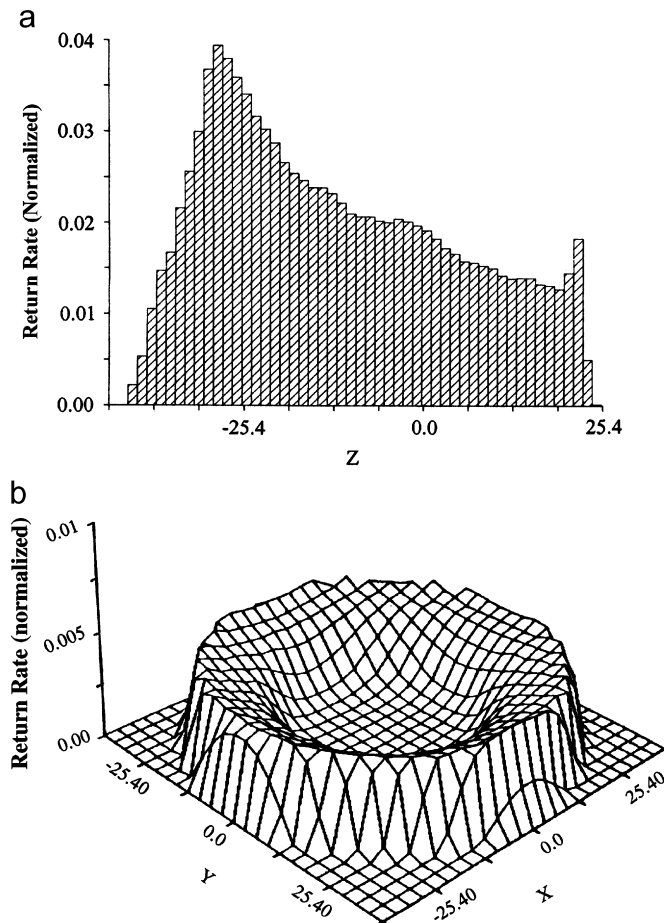
found in Fig. 8. Thus, the experimental flow fluid flow whose results are reported here is even more complex than a dynamical system on a three-dimensional torus. Such a higher dimensional description is consistent with the toroidal route to chaos of Ruelle and Taken (1971a, b), Newhouse et al. (1978), Ruelle (1979) and Takens (1980). The higher than three dimensionality is also consistent with the results of the Kolmogorov entropy production rate which showed an approximate embedding dimension of 24, see Fig. 5. Also important in this figure is the fact that the toroidal cross-section is filled in. (The torus becomes thickened.) This is evidence for the LMP jumping between members of the vertical stack of tori. It is also noticed for most values of θ that there are many values of $\dot\theta$ near zero. This arises from the fact that on the Poincaré section many returns do so with nearly zero up and down angular speed. These results are for high Reynolds numbers flow; they, nonetheless, provide evidence of unexpected coherence that might be expected only in simple dynamical systems.

We now present results for the frequency distribution $p(x, y, z)$ that the LMP has visited a given volume. The distribution $p(z) = \int p(x, y, z) \, dx \, dy$ for a vertical cross-section through the central shaft is displayed in Fig. 9a. Fig. 9b shows the (normalized) frequency density $p(x, y, z)$ at an x–y plane Poincaré section located at $z \approx 20$ cm above the bottom-sweeping impeller. The main feature of Fig. 9a and (b) is that the return rate (normalized) is not flat or uniform. This occurs because the flow is highly structured: consisting of the perimeter swirl and the stack of tori. The effect of non-uniformity

can be understood by first imagining the opposite extreme of LMP trajectories leading to a flat distribution. Consider a circular orbit, concentric to the impeller shaft in a plane perpendicular to the impeller shaft. Then any increase in velocity of the LMP along the orbit leads to a decrease in the time spent completing the orbit. This decrease, however, is exactly compensated by an increase in the frequency of return. A system of such orbits would yield a flat distribution no matter the speed. However, there is more to the story. The data of Fig. 9a show that the LMP is trapped most frequently near the impeller. That is, different regions of the flow trap the LMP for different lengths of time. An essential characteristic of the flow in the tank is that the flow paths are complicated. The tank flow system includes the perimeter flow and the stack of interior tori. The LMP can also jump from one torus to another. The different paths and their return rates provide a measure of the variation of the trapping ability of the tori in the tank flow. The same trapping phenomenon is observed in Fig. 9b, where it is seen that the tori system (perimeter swirl plus stack of smaller interior tori) attracts the LMP most of the time yielding an inhomogeneous distribution. Thus, the (normalized) return rate data reflect the relative strength with which different parts of the tori system attract the LMP. As previously noted in the experimental setup section, the LMP data set is as long as 100 h, sufficient to yield a flat average if there were one. Thus, the measured, non-uniform return rate distributions reflects the complexity and structure of the flow field.

At the left-hand side of Fig. 9a, the sharp rise of frequency in the region ($-38.1 \leqslant z \leqslant -25.4$ cm) is caused by the curvature of the bottom contour of the tank and the centrifugal pumping from the impeller. Prominent is the high frequency peak near $z \approx -28$ cm due to the recirculation near the impeller. Aside from this peak, the general trend is a decrease in frequency with minor peaks at $z \approx -3$, $z \approx -14$, $z \approx +9$ and $z \approx +14$ cm. This increased frequency of these local peaks can be associated with momentary trapping of the LMP in secondary flow tori. In Fig. 9b, the small values in the middle of the dog-bowl shaped distribution reflect the small frequency of finding the LMP in the central region of the tank. The distribution of the data on the plot indicate that the LMP passes more frequently through points near the wall of the tank, away from the center. This results in high frequency values near the wall giving a "dog bowl" shaped frequency distribution.

When the LMP is placed in the dead zone, it moves slowly in a spiral fashion towards the impeller. Indeed, it spends a long time in that region. However, very rarely does it enter the dead zone of its own accord. This is because the slowly moving dead zone is a region of higher relative pressure compared to the rapidly moving flow surrounding it. Thus, the LMP is effectively precluded from entering the dead zone from the outside.

The frequency distributions just described can be used in forming a SRB measure (Ruelle, 1979; Sinai, 1972a, b), $S = -p \ln p$ which is proportional to an entropy measure. This involves a simple transformation of the $p(x, y, z)$ data. In fact one can compute such a SRB measure in a plane perpendicular to the impeller shaft. The result is a dog-bowl shape similar to that shown in Fig. 9b which is not shown for brevity.

4.6. Eulerian microconductivity results

Visual observation of the evolution of dye streaks created by adding dye in the bottom perimeter tank gave streaks that filled the outer swirl and the adjacent toroidal sections before eventually filling in the central zone. To examine the characteristics of mixing at the center and perimeter of the tank and also the connection between the central region and the outer swirl flow, we used a microconductivity method. This measurement technique introduces a small quantity of passive, marker fluid and measures the time
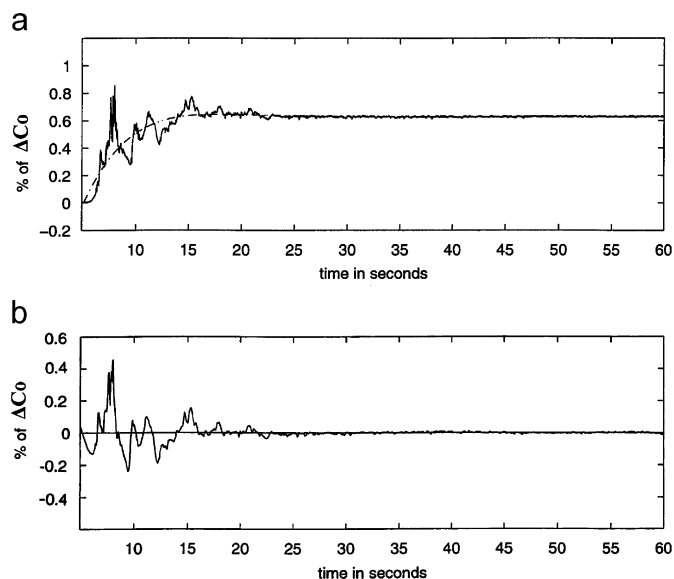

Fig. 10. Time series of concentration fluctuation in the upward swirl near the tank perimeter $r = 20$ cm. (a) Time evolution. (b) Time evolution but with running average removal. Large fluctuations occur for times less than 20 s.

history of the concentration fluctuations of the fluid at some other point in the fluid. Typically a salt or dye solution is used as the marker-body. Salt concentration can be detected using conductivity probes and dye concentration can be measured by light absorption or laser induced fluorescence (LIF).

Measurements were taken at two locations. Both measuring points were at 25 cm above the bottom of the tank and at radii of 10 and 20 cm from the center of the tank. This location is about 10 cm above the top of the impeller. The locations of the conductivity probes were chosen so that the probe at a radius of 10 cm was situated at the edge of the dead zone, whereas the probe at 20 cm provided data from the centrifugally driven up-welling swirl flow at the tank perimeter. Salt water of 1 l volume is suddenly introduced at the surface of the fresh water in the tank at a location close to the tank perimeter but on the opposite side of the impeller from the conductivity probes. The injected volume of salt water is broken up by the impeller motion and gradually distributed throughout the tank, including eventually, the dead zone. It takes about 5 s for small parcels of salt water to reach the region of the conductivity probe, subsequently there are large fluctuations of concentration and a gradual increase in the mean concentration level over time. For times greater than 30 s a steady-state develops with minimal concentration fluctuations.

Concentration time series data at $r = 20$ cm are presented in Fig. 10a. The time series for Fig. 10a shows a steady-state background concentration level of $C = 0.6\%$ of initial value ($C_0 = 100\%$) after 30 s. The 1 l volume of salt water is rapidly mixed to concentration levels of 1% by the time it takes to reach the conductivity probe. Fig. 10b shows the evolution of concentration fluctuations determined by subtracting the mean trend-line which is determined by a smooth, sixth-order polynomial fit to the data. Comparing Fig. 10a and b shows that the initial fluctuations are as large as the mean concentration levels. Subsequent concentration fluctuations decay exponentially in time: a similar exponential decay result is given in Tatterson (1991, Fig. 4.33, p. 232). An "event" is defined by the signal exceeding $1/e$ of its maximum. The conditional analysis of the concentration signal yields the distribution of the magnitude and duration of the events. Fig. 11 gives the number of events vs. their magnitude. Fig. 12 gives the number vs. the duration of the events.
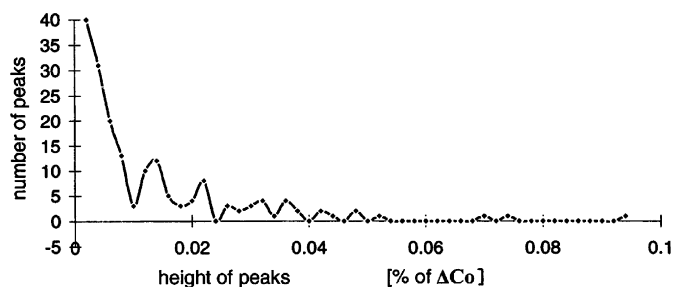
Fig. 11. Conditional analysis of conductivity (histogram: number vs. intensity) in the upward swirl near the tank perimeter. The intensity distribution of mixing events is related to the height of the peaks. Most common events are associated with smaller peaks.
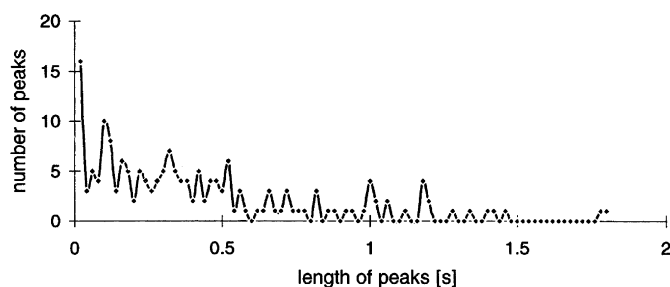

Fig. 12. Conditional analysis of conductivity (histogram: number vs. length of event) in the upward swirl near the tank perimeter. The duration of mixing events is related to the length in time of the peaks. Most common events are short lived.

Few events were larger than 0.03% C_0 in magnitude and most events occurred in less than 0.05 s. The largest fluctuation magnitude of 0.4% was longest in duration (approximately 4 s). That is, the most intense events were also the longest lived. Both the magnitude and duration of events decreased with increasing time.

Fig. 13a shows that the evolution of concentration fluctuations of the interior of the tank at $r = 10$ cm is a cumulative error function-like—a characteristic of diffusive processes. It is seen that the magnitude of concentration after 60 s reaches 0.6% which is the same level as in the perimeter zone seen in Fig. 10a. On comparing Figs. 10a and 13a it is seen that the concentration evolutions are quite different. Fig. 13a shows that the magnitude of concentration fluctuations is always small in the tank interior. This is shown explicitly by the time series of concentration fluctuations given in Fig. 13b. Evident in Fig. 13b is the absence of large fluctuations in the interior of the tank throughout the 60 s time series. This contrasts with the large fluctuations of the perimeter zone for time intervals less than 20 s seen in Fig. 10a. The differing evolution at the two locations suggests that the flow within the tank is structured.

5. Summary and conclusions

This study is motivated by the need to understand observations of inhomogeneous mixing in industrial crystallizers. Lagrangian marker particle (LMP) and microconductivity results are presented for measurements undertaken in a 280 l mixing tank with a single bottom-sweeping impeller. Values of Reynolds numbers are greater than 25,000 at the impeller tip. Long-time series of LMP trajectory data allows determination of the details of the circulation in the tank. The action of the impeller drives a rapidly moving upward-spiralling flow having a thickness of 9 cm at the tank perimeter. The flow returns slowly in a descending spiral through a series of secondary tori and through a quiescent region centered on the impeller. The radius of this quiescent region (called the dead zone) is about 7.6 cm.
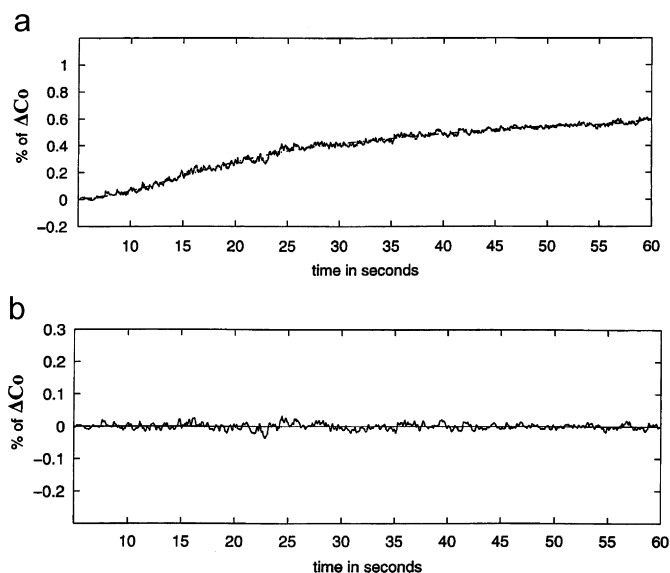
Fig. 13. Time series of concentration fluctuation at the center of the tank, $r = 10$ cm. (a) The concentration evolution is cumulative error function-like. (b) Evolution of concentration with running average removal. In both (a) and (b), there are no large concentration fluctuations at any time. This differs from the concentration evolution at the perimeter shown in Fig. 10b.

Measured return-rate distributions show that the LMP most frequently visits the impeller region and when it leaves it usually returns quickly. Much smaller frequencies of return are found in the center regions of the tank. Long return-times are associated with paths well above the bottom-sweeping impeller. This illustrates that flow structuring consisting of rapid and slow moving regions of flow occurs in the tank.

Conditional analysis of microconductivity signals reveals that the concentration fluctuations of added salt solution evolves differently in the central region and in the perimeter. In the central region, only small magnitude concentration fluctuations occur and the evolution of fluctuations is diffusive-like. In contrast, in the perimeter, large concentration fluctuations occur. Taken together, the LMP data and the microconductivity results suggests that rapid transport of scalar concentration occurs at the rapidly moving upwelling swirl along the tank perimeter. On the other hand, diffusive-like micromixing occurs in the slowly moving central region. The segregation of these regions leads to inhomogeneous mixing in the tank. This can be understood in light of the distinction between stirring and mixing discussed by Eckart (1948) and accounts for the observations of inhomogeneous mixing in these types of industrial crystallizers where crystallization reactions occur preferentially near the center of the bottom of the tank as opposed at the tank's perimeter.

The calculated Kolmogorov production rate $\dot{K}$ shows that the number of dimensions (of the dynamical system) necessary to account for the structure of the flow exceeds 20, thereby illustrating the (high) complexity of the flow. Nonetheless, surprising structure exists in this high Reynolds number flow. Vertical stacks of small horizontal tori, with an approximate radius of 2 cm concentric with the impeller axis, exist at loci of shear regions adjacent to the dead zone and the tank perimeter. Thus the flow in the tank is composed of a large torus of the perimeter swirl and downwelling flow enveloping stacks of smaller tori. The transfer of energy from the impeller involves flow on and between various tori in the tank. This is reflected in the form of the return-time distribution. Measured return-time distributions are found to comprise not just one clear distribution but a superposition of two log-normal distributions. One is composed of short return-times (0–10 s) corresponding to LMP

trajectories *along* the upward swirl and return flow. Longer return-times (up to 80 s) arise for LMP trajectories that move *through* the secondary tori. Furthermore, there is additional order to the flow as four sets of period doubling sub-sequences were discovered in the return-time distribution.

There are engineering implications of the results of our measurements. We suggest that in CSTRs with bottom-sweeping impellers, one will see changes in mixing as the secondary tori are sequentially formed as the tank is filled. Thus, the aspect ratio of the diameter to depth of the fluid in the tank is important. The aspect ratio and the tori structure can be used in an engineering design cycle to improve product quality and yield. In tanks with reactant feed jets near the impeller region, one can develop vertical concentration variations because of the presence of the secondary tori. These can affect, for instance, the particle size distribution in crystallizers. The greater frequency of return to the impeller region also implies that feed jets in this region will cause greater crystal growth in this region.

The experimental results presented here for high Reynolds number bottom-sweeping impeller tank flow support a description of the flow organized into tori as suggested by the Ruelle–Takens–Newhouse scenario. The present experimental approach consisting of LMP and microconductivity measurements allows the detection of this organization as well as the details of turbulent mixing on smaller scales. These two measurement methods give complimentary information which combine to give a more complete understanding of mixing in the bottom-sweeping impeller mixing tank.

Acknowledgments

References

Abarbanel, H.D.I., 1996. Analysis of Observed Chaotic Data. Springer, New York.

Abarbanel, H.D.I., Brown, R., Sidorowich, J.J., Tsimring, L.-Sh., 1993. The analysis of observed chaotic data in physical systems. Reviews of Modern Physics 65, 1331–1392.

Aitchison, J., Brown, J.A.C., 1966. The Lognormal Distribution. Cambridge University Press, Cambridge.

Andrieux, D., Gaspard, P., 2007. Entropy production and time asymmetry in non-equilibrium fluctuations. Physical Review Letters 98, 15060.

Aref, H., 1984. Stirring by chaotic advection. Journal of Fluid Mechanics 143, 1–21.

Aref, H., 1990. Chaotic advection of fluid particles. Philosophical Transactions of the Royal Society of London A 333, 273–288.

Aref, H., Balachandar, S., 1986. Physics of Fluids 29, 3515.

Aref, H., Jones, S.W., Thomas, O.M, 1988. Computers in Physics November/December, 22.

Batchelor, G.K., 1959. Small-scale variation of convected quantities like temperature in turbulent fluid. Journal of Fluid Mechanics 5, 113–139.

Bourne, J.R., Dell'ava, P., 1987. Micro- and macro-mixing in stirred tank reactors of different sizes. Chemical Engineering Research 65, 180–186.

Broomhead, D.S., King, G.P., 1986. Extracting qualitative dynamics from experimental data. Physica D 20, 217–236.

Broomhead, D.S., Jones, R., 1989. Time series analysis, fractals in the natural sciences. Proceedings of the Royal Society of London Series A 423, 103–121.

Dombre, T., Frisch, U., Greene, J.M., Henry, M., Mehr, A., Soward, M., 1986. Journal of Fluid Mechanics 167, 353.

Ducci, A., Yianneskis, M., 2005. Direct determination of energy dissipation in stirred vessels with two-point LDA. A.I.Ch.E. Journal 51, 2133–2149.

Eckart, C., 1948. An analysis of the stirring and mixing processes in incompressible fluids. Journal of Marine Research VII, 265–275.

Eckman, J.-P., Ruelle, D., 1985. Ergodic theory of chaos and strange attractors. Reviews of Modern Physics 57 (3), 61–6587.

Escudié, R., Liné, A., 2003. Experimental analysis of hydrodynamics in a radially stirred tank. A.I.Ch.E. Journal 49, 585–603.

Gilmore, R., 1998. Topological analysis of chaotic dynamical systems. Reviews of Modern Physics 70, 1455–1529.

Grassberger, P., Proccacia, I., 1983. Estimation of the Kolmogorov entropy from a chaotic signal. Physical Review A 28, 2591–2593.

Letellier, C., Aguirre, L.A., 2002. Investigating nonlinear dynamics from time series: the influence of symmetries and the choice of observables. Chaos 12, 549–558.

Letellier, C., Le Sceller, L., Dutertre, P., Gousbet, G., Fei, Z., Hudson, J.L., 1995. Topological characterization and global vector field reconstruction of an experimental electrochemical system. Journal of Physical Chemistry 99, 7016–7027.

Mañé, R., 1981. In: Lecture Notes in Mathematics, vol. 898. Springer, Berlin, pp. 230–254.

Maxey, M.R., 1988. The gravitational settling of aerosol particles in homogeneous turbulence and random flow fields. Journal of Fluid Mechanics 174, 441–465.

Maxey, M.R., Riley, J.J., 1983. Equation of motion for a small rigid sphere in a nonuniform flow. Physics of Fluids 26, 883–897.

McLaughlin, J.B., 1988. Particle size effects on Lagrangian turbulence. Physics of Fluids 31, 2544–2553.

Newhouse, S., Ruelle, D., Taken, F., 1978. Occurrence of strange Axiom A attractors near quasi periodic flows on T^m, $m \geqslant q3$. Communications in Mathematical Physics 64, 35–40.

Ottino, J.M., Leong, C.W., Rising, H., Swanson, P.D., 1988. Morphological structures produced by mixing in chaotic flows. Nature 333 (2), 419–425.

Reilly, C.D., Britter, R.E., 1985. Mixing times for passive tracers in stirred tanks. Proc. of the 5th European Conf. on Mixing, Wurzburg, pp. 356–375.

Ruelle, D., 1979. Sensitive dependence on initial conditions and turbulent behavior of dynamical systems. Annals of the New York Academy of Sciences 316, 408–416.

Ruelle, D., Taken, F., 1971a. On the nature of turbulence. Communications in Mathematical Physics 20, 167–192.

Ruelle, D., Takens, F., 1971b. Note concerning our paper: on the nature of turbulence. Communications in Mathematical Physics 23, 343–344.

Sharp, K.V., Adrian, R.J., 2001. PIV study of small-scale flow structure around a Rushton turbine. A.I.Ch.E. Journal 47, 766–778.

Sinai, Ya.G., 1972a. Uspekhi Matematicheskikh Nauk 27, 21–69.

Sinai, Ya.G., 1972b. Gibbs measures in ergodic theory. Russian Mathematical Surveys 27, 21–69.

Takens, F., 1980. Detecting strange attractors in turbulence. In: Rand, D.A., Young, L.S. (Eds.), Dynamical Systems and Turbulence, Warwick. Lecture Notes in Mathematics, vol. 898. Springer, Berlin, pp. 366–381.

Tatterson, G.B., 1991. Fluid Mixing and Gas Dispersion in Agitated Tanks. McGraw-Hill, NY.

Togatorop, A., Mann R., Scofield, D.F., 1994. An application of CFD to inert and reactive tracer mixing in a batch stirred vessel. In: A.I.Ch.E. Symposium Series, vol. 299, pp. 19–32.

Wittmer, S., 1996. Charactérization du mélange dans une cuve agitée par trajectographie. Thèse, L'Inst. Nat. Polytechnique de Lorraine, Nancy, France.